11

NEAR-FIELD TO FAR-FIELD TRANSFORMATION UTILIZING THE CONJUGATE GRADIENT METHOD

S. Ponnapalli

11.1 Introduction
11.2 Theory
A. Arbitrarily Shaped Antenna
B. Special Case of a Planar Current Distribution
C. Special Case of an Aperture in a Plane Conductor
D. Probe Compensation
11.3 Formulation of the Matrix Equation
11.4 CGFFT for Planar Measurements
11.5 Numerical Investigation
A. Uniform Arrays
B. Sinusoidal Current Distribution
C. Experimental Results
11.6 Conclusion
Acknowledgment
References

11.1 Introduction

Near-field antenna measurements have become widely used in antenna testing since they allow for accurate measurements of antenna patterns in a controlled environment. The earliest work in probe-compensated near-field measurements which utilizes modal expansions was performed in the early sixties by Brown and Jull [1] for cylindrical scanning in two dimensions and Kerns [2] for three dimensional planar

scanning. Probe-compensated spherical scanning formulas were developed by Jensen [3] in 1970. Wacker proposed a method to extract the modal coefficients for probe-compensated spherical measurements and a scheme to use the FFT to compute these coefficients [4-5]. Leach and Paris [6] extended the two dimensional cylindrical scanning theory to three dimensions in the early seventies. An overview of the development of near-field scanning techniques is found in [7] and Appel-Hansen presents a detailed description of planar, cylindrical and spherical scanning [8].

In this work, a new approach is presented in which near-field data over an arbitrary nonplanar surface is used to determine equivalent currents which exist over the entire aperture of the antenna. Given certain approximations, the currents should produce the correct far-fields in all regions in front of the antenna. For the results presented in this chapter, given the measured near-fields over an arbitrary nonplanar surface an equivalent planar source covering the actual antenna is determined. A method of moments procedure is used in which the equivalent currents on the planar source are discretized using rooftop basis functions in two orthogonal directions equally spaced on a plate whose minimum dimensions are greater than the maximum dimensions of the antenna. The electric field integral equation (EFIE) is formulated and a point matching procedure is used to express the known near-fields in terms of the unknown current amplitudes [9]. A matrix equation relating the near-fields at given points with the currents is then formulated as,

$$AQ = E \tag{1}$$

where Q represents the amplitudes of the unknown currents (which may be electric, magnetic, or both depending on the antenna) and E represents the electric field. If it is assumed that identical near-fields are generated from the planar source as those of the antenna under test, measured near-fields may be used for the right hand side of (1). The matrix equation is solved using CGM. If the number of field points exceeds the number of current patches, the matrix is rectangular and a least-squares solution is found without explicitly forming $A^H A$, where the superscript H denotes conjugate transpose, with computation of order MN when A is $\mathrm{M} \times \mathrm{N}$. The equivalent current approach has several advantages as compared with the modal expansion approach.

1. Even for antennas which are not highly directive, planar, cylindrical or any other geometry may be used for near-field measure-

ments since the far-fields outside the solid angle subtended by the particular geometry can be extrapolated. In the modal expansion method if a Fourier transform approach is used to compute the modal coefficients, then the fields outside the measurement plane are assumed to be zero for the planar case, and those outside of the cylindrical measurement surface are assumed to be zero for the cylindrical case. If a matrix method is used to compute the modal coefficients, the fields can be sampled on an arbitrarily shaped surface as long as the matrix is not singular or ill-conditioned. However, it is very difficult to incorporate probe compensation using the matrix method. Probe-compensation is considerably simpler to implement when the near-fields are measured over planar, cylindrical, or spherical surfaces. Therefore, for all practical purposes it is necessary to use spherical measurements to determine the far-fields over all elevation and azimuthal ranges. Spherical measurements require a complex test apparatus, and finding the modal coefficients is a computationally intense process. Using the equivalent current approach, with a similar order of computation as planar and cylindrical expansions, a similar accuracy in results as with spherical model expansions is obtained.

2. The near-field measurements may be made on an arbitrarily shaped surface, while still incorporating probe-compensation. Known errors in the positioning of the probe in planar, cylindrical or spherical geometries can be compensated for in the formulation.
3. An indication of the actual current distribution on the antenna is obtained. This may be useful for applications such as the location of faulty elements in an antenna array.
4. Electrically large probe antennas can be modeled in a simple manner.
5. In many cases, the maximum sample spacing is greater than the generally accepted maximum allowable spacings for planar, cylindrical and spherical scanning in the modal expansion method, when a Fourier transform is used to compute the coefficients.

The disadvantage of the equivalent current approach is that the matrix sizes can be prohibitively large as antenna size becomes large. To alleviate this problem, CGFFT may be applied. In planar scanning, if the number and spacing of the field points and current patches are chosen the same, the resulting matrix is square and is block Toeplitz. The structure of the matrix can be exploited by noting that a two

dimensional Fourier transform may be utilized to evaluate AP and $A^H R$ in CGM, where P is the search direction and R is the residual. This results in a tremendous decrease in storage and computation. The method has been called CGFFT and has previously been applied to scattering problems [10].

The theoretical basis for the equivalent current approach is detailed in section 11.2. The formulation of the matrix equation is detailed in section 11.3. The application of CGFFT is presented in section 11.4. Numerical results for several antenna configurations are presented in section 11.5.

11.2 THEORY

A. Arbitrarily Shaped Antenna

Consider an arbitrarily shaped antenna radiating into free space. Let the antenna be surrounded by a "box" with surface Σ. The surface S_0 is a plane which encompasses the aperture of the antenna, as shown in Fig. 11.1a. To find equivalent currents on the surface Σ which radiate the same fields $(\overline{E}, \overline{H})$ external to the box, let us postulate zero fields inside the box. To support such fields, equivalent currents must exist on Σ which are,

$$\overline{J} = \overline{n} \; X \; \overline{H} \; on \; \Sigma \tag{2a}$$

$$\overline{M} = \overline{E} \; X \; \overline{n} \; on \; \Sigma \tag{2b}$$

as shown in Fig. 11.1b. These currents radiate identical fields external to the box as the original source. It is further assumed that the fields external to the box on Σ are zero on all surfaces of the box except S_0, then $\overline{J}$ and $\overline{M}$ exist only on S_0. This amounts to assuming that the leakage and backward radiation from the antenna is negligible. Since it is assumed that $\overline{E}$ and $\overline{H}$ are zero inside the box, we can replace it by free space. Then $\overline{J}$ and $\overline{M}$ radiate into free space as shown in Fig. 11.1c. We can then use measured near-fields to determine $\overline{J}$ and $\overline{M}$.

B. Special Case of a Planar Current Distribution

Consider a planar current distribution as shown in Fig. 11.2a, where Σ is the plane containing the currents, and S_0 encompasses the entire current distribution. Let us postulate the original fields $(\overline{E}, \overline{H})$

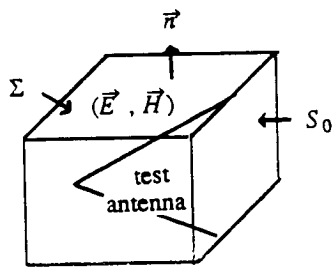

Figure 1a.

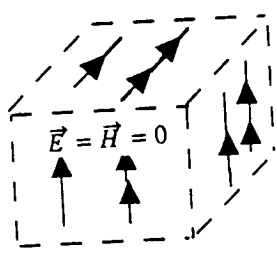

Figure 1b.

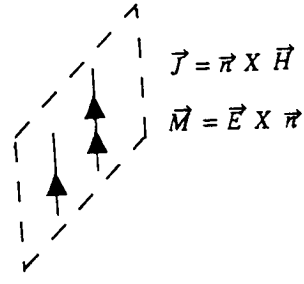

Figure 1c.

Figure 11.1 Arbitrarily shaped antenna.

in the right-half plane, and zero fields in the left-half plane. There can be no tangential component of $\overline{H}$ in any plane containing the electric currents [11]. Therefore, to support such fields, equivalent currents must exist on Σ which are,

$$\overline{J} = \overline{n} \; X \; \overline{H} \; on \; S_0 \tag{3a}$$

$$\overline{M} = \overline{E} \; X \; \overline{n} \; on \; \Sigma \tag{3b}$$

These currents radiate identical fields in the right-half plane as the original source. If we place a perfect magnetic conductor as shown in Fig. 11.2b, then the magnetic currents are "shorted out". Then using image theory, we can express $\overline{J}$ as,

$$\overline{J} = 2\overline{n} \; X \; \overline{H} \; on \; S_0 \tag{4}$$

where $\overline{J}$ radiates into free space as shown in Fig. 11.1c. We can now use measured near-fields to determine $\overline{J}$.

C. Special Case of an Aperture in a Plane Conductor

Consider a planar aperture as shown in Fig. 11.3a, where Σ is the plane containing the conductor, and S_0 encompasses the entire aperture. Let us postulate the original fields $(\overline{E}, \overline{H})$ in the right-half plane, and zero fields in the left-half plane. The tangential components of $\overline{E}$ and $\overline{H}$ on the conducting plane are zero. Therefore, to support such fields, equivalent currents must exist on Σ which are,

$$\overline{J} = \overline{n} \; X \; \overline{H} \; on \; S_0 \tag{5a}$$

$$\overline{M} = \overline{E} \; X \; \overline{n} \; on \; S_0 \tag{5b}$$

These currents radiate identical fields in the right-hand plane as the original source. If we place a perfect electric conductor over the aperture as shown in Fig. 11.3b, then the electric currents are "shorted out". Then using image theory, we can express $\overline{M}$ as,

$$\overline{M} = 2\overline{E} \; X \; \overline{n} \; on \; S_0 \tag{6}$$

where $\overline{M}$ radiate into free space as shown in Fig. 11.3c. We can now use measured near-fields to determine $\overline{M}$.

From Sections A, B and C it is clear that the solution for an arbitrary antenna is the superposition of that of the planar current case,

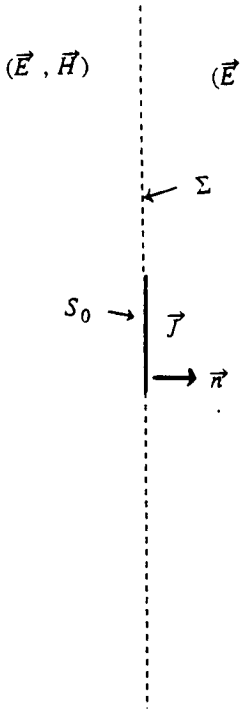

Figure 2a.

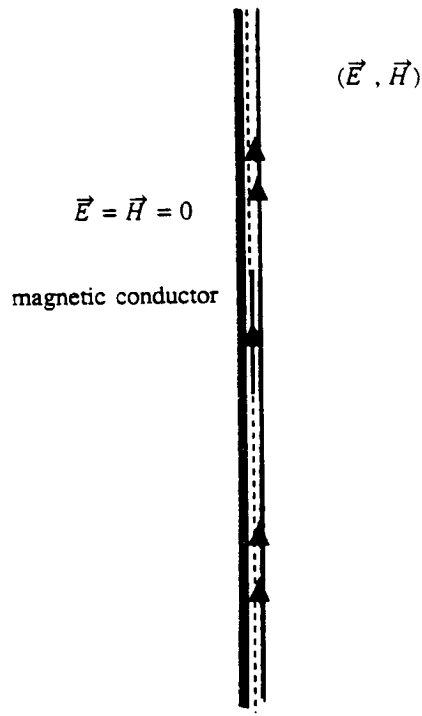

Figure 2b.

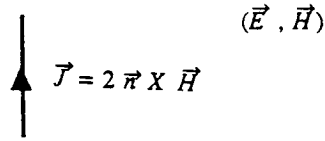

Figure 2c.

Figure 11.2 Planar current distribution.

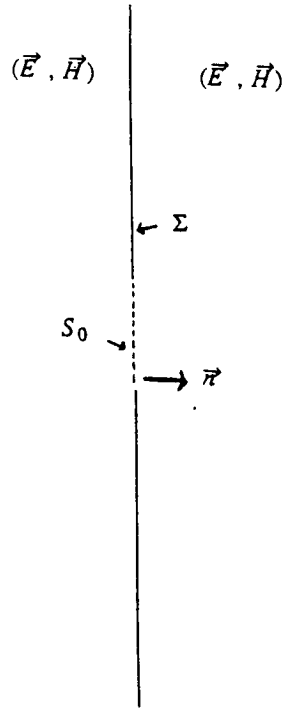

Figure 3a.

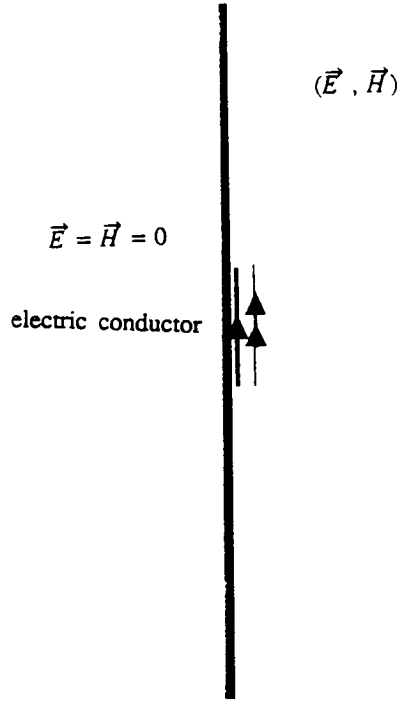

Figure 3b.

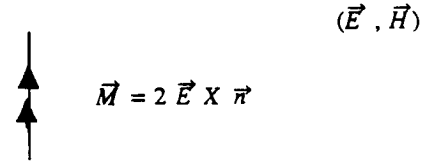

Figure 3c

Figure 11.3 Planar aperture distribution.

and the planar aperture case. In the remainder of this chapter, planar currents are dealt with. Analogous formulations for apertures can be found, and a superposition of the two will result in the formulation for arbitrary antennas.

D. Probe Compensation

Consider case (B) where the planar currents have been replaced by equivalent electric currents, and a probe has been placed in the right-half plane in order to measure the near-fields radiated by the test antenna. Let the principle fields radiated by the test antenna be $\overline{E}_a$ and those radiated by the probe be $\overline{E}_b$. Let the fields scattered by the probe when the test antenna is turned on be $\overline{E}_{as}$. Similar definitions apply for the currents on the test antenna and the probe $\overline{J}_a$, $\overline{J}_{as}$, $\overline{J}_b$, and $\overline{J}_{bs}$. The amplitudes of the near-field data are obtained by measuring the voltage across a load on the terminals of the probe. This voltage is proportional to the open-circuit received voltage on the probe. To within a constant of proportionality, the received signal when the probe is positioned at $\bar{r}_0$ is [12-13],

$$P_B(\bar{r}_0) \triangleq \int_V \left(\overline{E}_a \cdot \overline{J}_b - \overline{E}_b \cdot \overline{J}_{bs}\right) dV \tag{7}$$

The second term on the right arises from the induced current on the test antenna due to the presence of the probe. If this term is neglected,

$$P_B(\bar{r}_0) \approx \int_V \overline{E}_b \cdot \overline{J}_a dV = \int_V \overline{E}_a \cdot \overline{J}_b dV \tag{8}$$

One can approximate the currents on the probe with known basis functions and determine $\overline{J}_b$. If the probe is assumed to be an ideal Hertzian dipole located at (x_f, y_f, z_f), the current $\overline{J}_b$ is,

$$\overline{J}_b = \delta(x' - x_f)\delta(y' - y_f)\delta(z' - z_f) \tag{9}$$

Then evaluating (8) is equivalent to finding the scattered fields due to $\overline{J}_a$ at a point (x_f, y_f, z_f) in the $\hat{a}_b$ direction from,

$$P_B(\bar{r}_0) = E(x_f, y_f, z_f) \cdot \hat{a}_b \tag{10}$$

$$P_B(\bar{r}_0) = (-j\omega\mu - \nabla\phi) \cdot \hat{a}_b \tag{11}$$

If a method of moments procedure is used to discretize $\overline{J}_a$ in terms of known basis functions, then (11) is equivalent to using a point matching procedure to form a matrix equation. The formulation is detailed in Section 11.3.

Probe-compensation can be incorporated using a method of moments procedure, without neglecting the currents induced on the test antenna due to the probe or the interaction between the induced currents and the induced fields (referred to as multiple reflections). When the planar current $\overline{J}_a$ and the current on the probe $\overline{J}_b$ are discretized in terms of known basis functions with unknown coefficients, a moment matrix $[Z_{ab}]$ can be formed. For example,

$$< \overline{E}_a, \overline{J}_b >= [Z_{ab}][I_a] \tag{12}$$

Here, $< \overline{E}_a, \overline{J}_b >$ is the reaction of $\overline{E}_a$ on $\overline{J}_b$ and is given by (8).

Consider the case when the test antenna alone is radiating into free space and is excited by $[V_1]$.

$$[Z_{aa}][I'_a] = [V_1] \tag{13}$$

$[Z_{aa}]$ is the self-impedance matrix of the equivalent sources, and I'_a are the equivalent sources. These are the currents which are required to compute the correct far-fields.

Now consider the test antenna in the presence of the probe as shown in Fig. 11.4. The probe may be electrically large. From network theory,

$$\begin{bmatrix} [Z_{aa}] & [Z_{ab}] \\ [Z_{ba}] & [Z_{bb}] \end{bmatrix} \begin{bmatrix} [I_a] \\ [I_b] \end{bmatrix} = \begin{bmatrix} [V_1] \\ [V_2] \end{bmatrix} \tag{14}$$

$[Z_{bb}]$ is the self-impedance matrix of the probe. It is a diagonal matrix whose elements are the impedance seen through the terminals of the probe when it is located at each measurement position. Each of the elements may be approximated to be the same. If the excitation $[V_1]$ is the same in the cases with and without the probe,

$$\begin{bmatrix} [Z_{aa}] & [Z_{ab}] \\ [Z_{ba}] & [Z_{bb}] \end{bmatrix} \begin{bmatrix} [I_a] \\ [I_b] \end{bmatrix} = \begin{bmatrix} [Z_{aa}]\ [I'_a] \\ [V_2] \end{bmatrix} \tag{15}$$

From Thevenin's and Norton's equivalent circuits, if a load impedance Z_L is placed across the terminals of the probe, the voltage across the

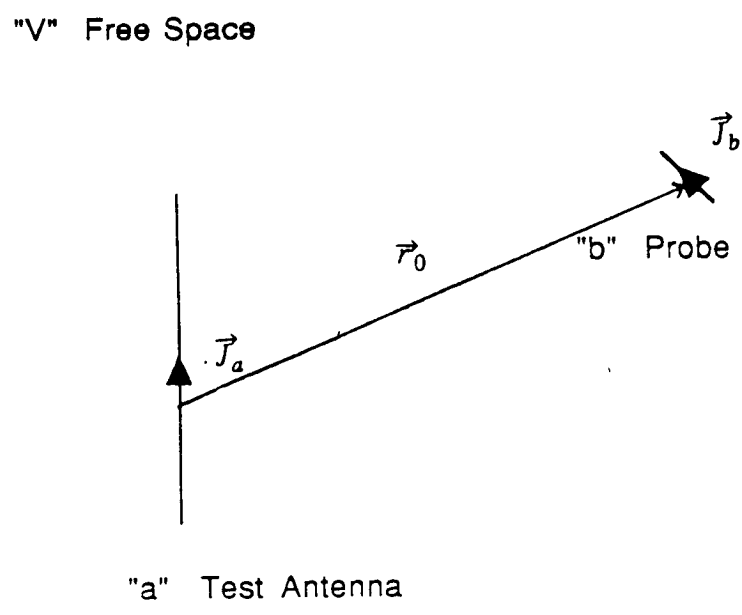

Figure 11.4 Probe compensation geometry.

load is,

$$V_L = \frac{Z_L}{Z_{bb} + Z_L} V_{oc}$$
$$= \frac{-Z_{bb} Z_L}{Z_{bb} + Z_L} I_{sc} \tag{16}$$

Therefore the signal on the probe to within a constant of proportionality is,

$$P_B(\bar{r}_0) = -Z_{bb} I_b \,|_{V_2=0} \tag{17}$$

From (15) and (17),

$$[Z_{aa}]\left([I_a] - [I'_a]\right) = [Z_{ab}][Z_{bb}]^{-1}[P_B(\bar{r}_0)] \tag{18}$$

$$[Z_{aa}][I_a] = [P_B(\bar{r}_0)] \tag{19}$$

Equations (18) and (19) can be solved for $[I'_a]$. By utilizing $[I'_a]$ to compute the far-fields, the effects of all induced currents are removed.

11.3 Formulation of Matrix Equation

Consider the equivalent source distribution to be a plate in the $x-z$ plane composed of equally spaced rooftop function representations for the currents. The currents are given by,

$$\overline{J} = \hat{a}_x \sum_{i=1}^{M}\sum_{j=1}^{N} \alpha_{ij} P_x(x_i, z_j) + \hat{a}_z \sum_{i=1}^{M}\sum_{j=1}^{N} \beta_{ij} P_z(x_i, z_j) \tag{20}$$

where P are rooftop functions, with P_x defined as,

$$\begin{aligned} P_x(x_i, z_j) &= \frac{(x - x_i)}{\Delta x} + 1 \begin{cases} x_i - \Delta x < x \le x_i \\ z_j - \Delta z/2 < z \le z_j + \Delta z/2 \end{cases} \\ &= \frac{-(x - x_i)}{\Delta x} + 1 \begin{cases} x_i < x \le x_i + \Delta x \\ z_j - \Delta z/2 < z \le z_j + \Delta z/2 \end{cases} \\ &= 0, \qquad \text{otherwise} \end{aligned} \tag{21}$$

and P_z defined as,

$$\begin{aligned} P_z(x_i, z_j) &= \frac{(z - z_j)}{\Delta z} + 1 \begin{cases} z_j - \Delta z < z \le z_j \\ x_i - \Delta x/2 < x \le x_i + \Delta x/2 \end{cases} \\ &= \frac{-(z - z_j)}{\Delta x} + 1 \begin{cases} z_j < z \le z_j + \Delta z \\ x_i - \Delta x/2 < x \le x_i + \Delta x/2 \end{cases} \\ &= 0, \qquad \text{otherwise} \end{aligned} \tag{22}$$

α_{ij} and β_{ij} are the unknown coefficients to be solved for. The field at any point (x_f, y_f, z_f) can be found from,

$$\begin{aligned} \overline{E}(x_f, y_f, z_f) = -j\omega\mu \Bigg[&\sum_{k=1}^{M}\sum_{l=1}^{N} \overline{J}(k,l) \iint g(\overline{r} - \overline{r}'_{kl}) ds'_{kl} \\ &- \frac{1}{k_0^2} \iint \nabla' \cdot \overline{J}(k,l) \nabla' g(\overline{r} - \overline{r}'_{kl}) ds'_{kl} \Bigg] \end{aligned} \tag{23}$$

where, g is the three dimensional Green's function,

$$g(\overline{r} - \overline{r}'_{kl}) = g(x, y, z, x', z') = \frac{e^{-jkR}}{4\pi R} \tag{24}$$

$$R = \left[(x - x')^2 + (y)^2 + (z - z')^2\right]^{1/2} \tag{25}$$

The first term due to the vector potential may be simply evaluated by approximating the rooftop functions to be pulses where the integration is performed over the kl^{th} current patch. The second term due to the charge may be evaluated by finding the divergence of the current from (20) using,

$$\nabla' \cdot \overline{J} = \hat{a}_x \sum_{i=1}^{M} \sum_{j=1}^{N} \alpha_{ij} \frac{\partial P_x(x_i, z_j)}{\partial x'} + \hat{a}_z \sum_{i=1}^{M} \sum_{j=1}^{N} \beta_{ij} \frac{\partial P_z(x_i, z_j)}{\partial z'} \tag{26}$$

Defining the coordinate of the center of each current patch as (x_k, y_l) and the following points,

$$\begin{aligned} x_s &= x_k - \Delta x/2 \qquad x_e = x_k + \Delta x/2 \\ z_s &= z_l - \Delta z/2 \qquad z_e = z_l + \Delta z/2 \\ x_1 &= x_k - \Delta x \qquad x_2 = x_k \qquad x_3 = x_k + \Delta x \\ z_1 &= z_l - \Delta z \qquad z_2 = z_l \qquad z_3 = z_l + \Delta z \end{aligned}$$

The components of the field at a point (x_f, y_f, z_f) can be found. The x-component of the field is,

$$E_x(x_f, y_f, z_f) = -j\omega\mu \left[E^A(J_x) + E_x^P(J_x) + E_x^P(J_z)\right] \tag{28}$$

where E^A which represents the field due to the magnetic potential term is given by,

$$E^A(J_x) = \sum_{k=1}^{M} \sum_{l=1}^{N} \alpha_{kl} \int_{x'=x_s}^{x_e} \int_{z'=z_s}^{z_e} g\left(\overline{r} - \overline{r}'_{kl}\right) dx' dz' \tag{29}$$

where, E_P represents the fields due to the scalar potential term and are given by,

$$\begin{aligned} E_x^P(J_x) = & \frac{1}{k_0^2 \Delta x} \sum_{k=1}^{M} \sum_{l=1}^{N} \alpha_{kl} \\ & \int_{zs}^{ze} \left[g(xf, yf, zf, x3, z') + g(xf, yf, zf, x1, z') \right. \\ & \left. - 2g(xf, yf, zf, x2, z')\right] dz' \end{aligned} \tag{30}$$

$$E_x^P(J_z) = \frac{1}{k_0^2 \Delta z} \sum_{k=1}^{M} \sum_{l=1}^{N} \beta_{kl} \left[\int_{z2}^{z3} [g(xf, yf, zf, xe, z') - g(xf, yf, zf, xs, z')]\, dz' - \int_{z1}^{z2} [g(xf, yf, zf, xe, z') - g(xf, yf, zf, xs, z')]\, dz' \right] \tag{31}$$

The y-component of the field is,

$$E_y(x_f, y_f, z_f) = -j\omega\mu[E_y^P(J_x) + E_y^P(J_z)] \tag{32}$$

where,

$$E_y^P(J_x) = \frac{1}{k_0^2 \Delta x} \sum_{k=1}^{M} \sum_{l=1}^{N} \alpha_{kl} \int_{xs}^{xe} \left[\int_{x2}^{x3} g_y(xf, yf, zf, x', z')\, dx' - \int_{x1}^{x2} g_y(xf, yf, zf, x', z')\, dx' \right] dz' \tag{33}$$

$$E_y^P(J_z) = \frac{1}{k_0^2 \Delta z} \sum_{k=1}^{M} \sum_{l=1}^{N} \beta_{kl} \int_{xs}^{xe} \left[\int_{z2}^{z3} g_y(xf, yf, zf, x', z')\, dz' - \int_{z1}^{z2} g_y(xf, yf, zf, x', z')\, dz' \right] dx' \tag{34}$$

with,

$$g_y(x, y, z, x', z') = \frac{e^{-jkR}}{4\pi R^2}(y - y') \left(jk + \frac{1}{r} \right) \tag{35}$$

The z-component of the field is,

$$E_z(x_f, y_f, z_f) = -j\omega\mu \left[E^A(J_z) + E_z^P(J_x) + E_z^P(J_z) \right] \tag{36}$$

where,

$$E^A(J_z) = \sum_{k=1}^{M} \sum_{l=1}^{N} \beta_{kl} \int_{z_s}^{z_e} \int_{x_s}^{x_e} g\left(\overline{r} - \overline{r}'_{kl}\right) dx'\, dz' \tag{37}$$

$$E_z^P(J_x) = \frac{1}{k_0^2 \Delta x} \sum_{k=1}^{M} \sum_{l=1}^{N} \alpha_{kl} \left[\int_{x2}^{x3} [g(xf, yf, zf, x', ze) - g(xf, yf, zf, x', zs)]\, dx' - \int_{x1}^{x2} [g(xf, yf, zf, x', ze) - g(xf, yf, zf, x', zs)]\, dx' \right] \tag{38}$$

$$E_z^P(J_z) = \frac{1}{k_0^2 \Delta z} \sum_{k=1}^{M} \sum_{l=1}^{N} \beta_{kl} \int_{xs}^{xe} [g(xf, yf, zf, x', z3) + g(xf, yf, zf, x', z1) - 2g(xf, yf, zf, x', z2)\, dx'] \tag{39}$$

Equations (28), (32) and (36) represent the EFIE, and when a point matching procedure is used, a component of the electric field in any direction at the given point may be found. This is proportional to the signal on a probe measuring the electric field in that direction, when it is assumed that the probe is a small dipole. For the special cases of planar, cylindrical and spherical scanning, the following matrix equations are obtained –

$$\begin{bmatrix} E_x(J_x) & E_x(J_z) \\ E_z(J_x) & E_z(J_z) \end{bmatrix} \begin{bmatrix} J_x \\ J_z \end{bmatrix} = \begin{bmatrix} E_x(x_f, y_f, z_f) \\ E_z(x_f, y_f, z_f) \end{bmatrix} \tag{40}$$

for planar scanning,

$$\begin{bmatrix} E_\phi(J_x) & E_\phi(J_z) \\ E_z(J_x) & E_z(J_z) \end{bmatrix} \begin{bmatrix} J_x \\ J_z \end{bmatrix} = \begin{bmatrix} E_\phi(x_f, y_f, z_f) \\ E_z(x_f, y_f, z_f) \end{bmatrix} \tag{41}$$

for cylindrical scanning, and

$$\begin{bmatrix} E_\theta(J_x) & E_\theta(J_z) \\ E_\phi(J_x) & E_\phi(J_z) \end{bmatrix} \begin{bmatrix} J_x \\ J_z \end{bmatrix} = \begin{bmatrix} E_\theta(x_f, y_f, z_f) \\ E_\phi(x_f, y_f, z_f) \end{bmatrix} \tag{42}$$

for spherical scanning. In (40), the various blocks of the matrix are,

$$E_x(J_x) = E^A(J_x) + E_x^P(J_x) \tag{43}$$

$$E_x(J_z) = E_x^P(J_z) \tag{44}$$

$$E_z(J_x) = E_z^P(J_x) \tag{45}$$

$$E_z(J_z) = E^A(J_z) + E_z^P(J_z) \tag{46}$$

The E^A and E^P terms are defined in (29)-(31), (33)-(34) and (37)-(39). The relationship of E_ϕ and E_θ with E_x, E_y and E_z are given in [11]. For example, consider $E_\phi(J_x)$,

$$E_\phi(J_x) = -E_x(J_x)\sin\phi + E_y(J_x)\cos\phi \tag{47}$$

with

$$\sin\phi = \frac{y_f}{x_f^2 + y_f^2}$$
$$\cos\phi = \frac{x_f}{x_f^2 + y_f^2} \tag{48}$$

The matrix equation is solved using CGM (case A), the algorithm for which is outlined in [14].

11.4 CGFFT For Planar Measurements

In planar measurements in which the plane containing the current patches and that over which the field points are taken are parallel, and of the same size, the computation and storage requirements can be tremendously reduced by using CGFFT. Most of the computation at each iteration in CGM occurs in the calculation of $A\,P$ and $A^H\,R$, where P is the search direction and R is the residual. When the discretization of the current patches and field points is chosen to be equal, the resulting matrix is block Toeplitz. In this case, $A\,P$ and $A^H\,R$ represent discrete convolutions, and can be evaluated by multiplying their discrete Fourier transforms and inverse Fourier transforming the result [15]. This can be performed efficiently using a two dimensional FFT.

Consider the matrix equation (40), which must be evaluated when computing AP or AJ. This is of the form,

$$\begin{bmatrix} E_x(J_x) & E_x(J_z) \\ E_z(J_x) & E_z(J_z) \end{bmatrix} \begin{bmatrix} P_x \\ P_z \end{bmatrix} = \begin{bmatrix} AP_x(x_f, y_f, z_f) \\ AP_z(x_f, y_f, z_f) \end{bmatrix} \tag{49}$$

Then $[AP_x]$ can be found from,

$$[AP_x] = F_\tau^{-1}\Big\{ F\{[E_x(J_x)]_p\}\, F\{[P_x]_0\} + F\{[E_x(J_z)]_p\}\, F\{[P_z]_0\} \Big\} \tag{50}$$

and $[AP_z]$ can be found from,

$$[AP_z] = F_\tau^{-1}\Big\{F\{[E_z(J_x)]_p\}\,F\{[P_x]_0\} + F\{[E_z(J_z)]_p\}\,F\{[P_z]_0\}\Big\} \tag{51}$$

Here F denotes a two dimensional discrete Fourier transform and F^{-1} is a two-dimensional inverse discrete Fourier transform. The subscript p denotes a periodic extension of the matrix, the subscript 0 denotes the matrix with zero padding, and the subscript τ denotes the truncation operator. The adjoint operator is also required to compute $A^H R$. This is given by,

$$\begin{bmatrix} E_x^H(J_x) & E_z^H(J_x) \\ E_x^H(J_z) & E_z^H(J_z) \end{bmatrix} \begin{bmatrix} R_x \\ R_z \end{bmatrix} = \begin{bmatrix} A^H R_x(x_f, y_f, z_f) \\ A^H R_z(x_f, y_f, z_f) \end{bmatrix} \tag{52}$$

From (52) $[A^H R_x]$ is computed using,

$$[A^H R_x] = F^{-1}\Big\{F\{[E_x^*(J_x)]_p\}\,F\{[R_x]_0\} + F\{[E_z^H(J_x)]_p\}\,F\{[R_z]_0\}\Big\} \tag{53}$$

and $[A^H R_z]$ can be computed using,

$$[A^H R_z] = F_\tau^{-1}\Big\{F\{[E_x^H(J_z)]_p\}\,F\{[R_x]_0\} + F\{[E_z^*(J_z)]_p\}\,F\{[R_z]_0\}\Big\} \tag{54}$$

where the superscript $*$ denotes conjugate. In (53) and (54) use has been made of the fact that $E_x(J_x)$ and $E_z(J_z)$ are both symmetric matrices, and their Hermitian is simply the conjugate of the matrices.

Using CGFFT, for $N\ X\ N$ measured field points, six matrices of size $(2N-1)\times(2N-1)$, namely $E_x(J_x)$, $E_x(J_z)$, $E_z(J_x)$, $E_z(J_z)$, $E_x^H(J_z)$ and $E_z^H(J_x)$ need to be stored. If a matrix method in modal expansions is used, $2N^2\ X\ 2N^2$ elements need to be stored.

The required computation for the two dimensional FFTs is $(2N-1)^2\log_2(2N-1)$ and each iteration requires six such operations. For

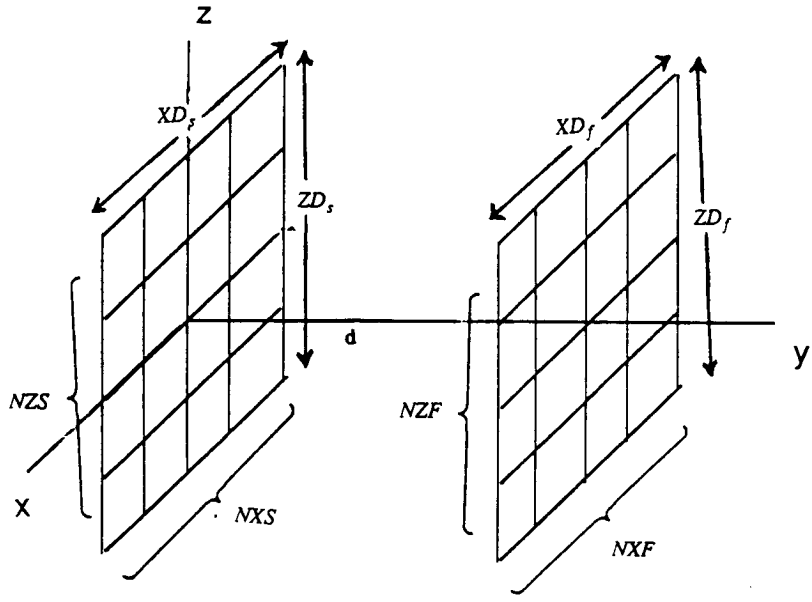

Figure 11.5 Planar measurements geometry.

the purpose of comparison of computation with the modal expansion method, assume a sample spacing of 0.5λ and a square planar surface for the currents of dimension $2a$ where a is the smallest radius circumscribing the antenna aperture. (This may be a much larger area than what is actually required.) Then $\frac{4a}{\lambda}$ or $\frac{2ka}{\pi}$ current patches are required and the order of computation under these conditions using CGFFT is $(ka)^2 \log_2(\frac{4ka}{\pi})$. The order of computation would differ if the size of the plane or the sample spacing are varied. This is comparable to the $(ka)^2 \log_2(ka)$ order of computation required to compute the entire far-fields using planar or cylindrical modal expansions.

11.5 Numerical Investigation

Far-field results for several planar antenna configurations are presented in this section. In all examples where planar near-fields are used, CGFFT has been employed. For planar measurements, the pertinent parameters which are referred to are shown in Fig. 11.5. Similar definitions apply for cylindrical measurements with *NPHIF* being the number of points measured in the ϕ direction.

In sections A and B, synthetic near-field data is used, and a com-

parison is made with analytic far-fields. Section C utilizes experimental results for a microstrip array, and results are compared with far-fields obtained using modal expansions.

A. Uniform Arrays

A uniform array in the x-z plane has a far-field pattern,

$$F(\theta, \phi) = \sin\theta \frac{\sin\left[\frac{N_x \Psi_x}{2}\right]}{\sin\left(\frac{\Psi_x}{2}\right)} \sin\theta \frac{\sin\left[\frac{N_z \Psi_z}{2}\right]}{\sin\left(\frac{\Psi_z}{2}\right)} \tag{55}$$

where,

$$\Psi_x = k\Delta x \sin\theta \cos\phi + \delta_x \tag{56a}$$

$$\Psi_z = k\Delta z \cos\theta + \delta_z \tag{56b}$$

where Δx and Δz are the spacing between the dipoles in the x and z directions, N_x and N_z are the number of dipoles in the x and z directions and δ_x and δ_z are the progressive phase shifts of the currents in the x and z directions.

Example 1

$$\Delta x = \Delta z = 4\lambda$$
$$N_x = N_z = 2$$
$$\delta_x = \delta_z = 0$$

Planar measurements:

$$XD_s = ZD_s = XD_f = ZD_f = 4.5\lambda$$
$$d = 30\lambda$$
$$NXS = NZS = NXF = NZF = 15$$

It should be noted that for this example when modal expansions are used, the cutoff angle θ_c beyond which the far-fields cannot be determined is $0.5°$. The cutoff angle is approximated by [16],

$$\theta_c \approx \tan^{-1}\left[\frac{ZD_f - \Delta z}{2d}\right] \tag{57}$$

In the equivalent current approach, the angle θ over which the near-field is sampled is varied between 85.7° and 94.3° for $\phi = 90°$. Figure 11.6 shows $|E_\theta|$ versus θ in dB for $\phi = 90°$. Far fields are very accurate up to $\pm 40°$ of $\theta = 90°$ and to within approximately 5 dB over the entire elevation range. A good extrapolation of the far-fields is obtained. Figures 11.7 and 11.8 show the normalized z and x directed current densities, respectively. The equivalent currents very accurately represent the actual currents. J_x is negligible and J_z reflects the delta function distribution.

Example 2

$$\Delta x = \Delta z = 4\lambda$$
$$N_x = N_z = 2$$
$$\delta_x = \delta_z = 0$$

Parabolic surface:

$$XD_s = ZD_s = ZD_f = 4.5\lambda$$
$$NXS = NZS = NPHIF = NZF = 15$$

The equation of the parabola is,

$$y = -0.0167x^2 + 30 \tag{58}$$

This example demonstrates that accurate far-fields are obtained when a measurement surface other than planar, cylindrical or spherical is used. The near-fields are sampled over a surface which is parabolic in the $x-y$ plane and constant in the $y-z$ plane. Figure 11.9 shows $|E_\theta|$ versus θ in dB for $\phi = 90°$. Results with about the same accuracy as the planar measurement case are obtained.

Example 3

$$\Delta x = \Delta z = 6\lambda$$
$$N_x = N_z = 2$$
$$\delta_x = \delta_z = 0$$

Cylindrical measurements:

$$XD_s = ZD_s = 6.5\lambda$$

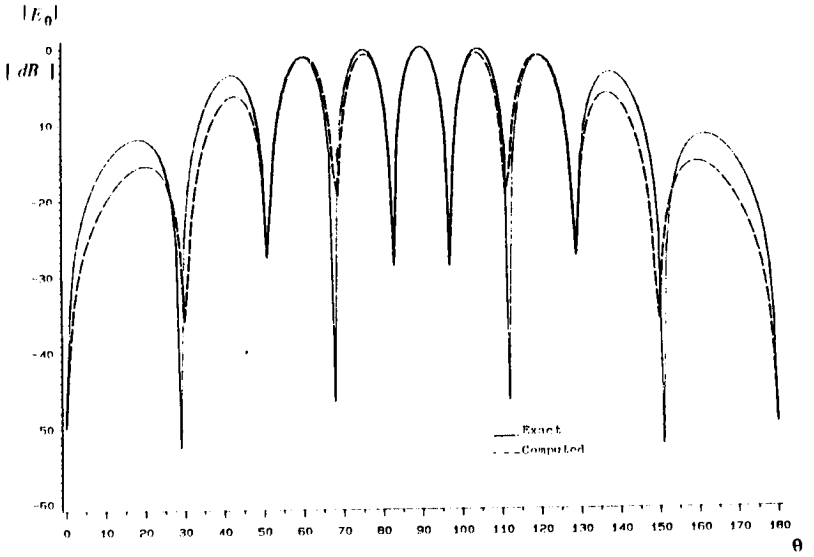

Figure 11.6 Comparison of exact and computed far-fields for $\phi = 90$ cut for 2×2 dipoles on a $4\lambda \times 4\lambda$ surface using planar scanning.

$$0 \leq \phi_f \leq \pi,\ ZD_f \text{ is varied}$$
$$\rho_0 = 12\lambda$$
$$NXS = NZS = 25$$
$$NPHIF = 23, NZF = 64$$

In this example, the required sampling rate when the equivalent current approach is used is investigated. The discretization in the ϕ direction is approximately 0.59λ, which is greater than $\lambda/2\rho(0.12\lambda)$ where ρ is the radius of the smallest cylinder circumscribing the array centered at the origin. The discretization in the z direction is varied as $1\lambda, 1.5\lambda$ and 2.5λ. Figure 11.10 shows $|E_\theta|$ versus θ in dB for $\phi = 90°$. In all three cases, the far-fields obtained by the equivalent current approach agree well with the exact far-field.

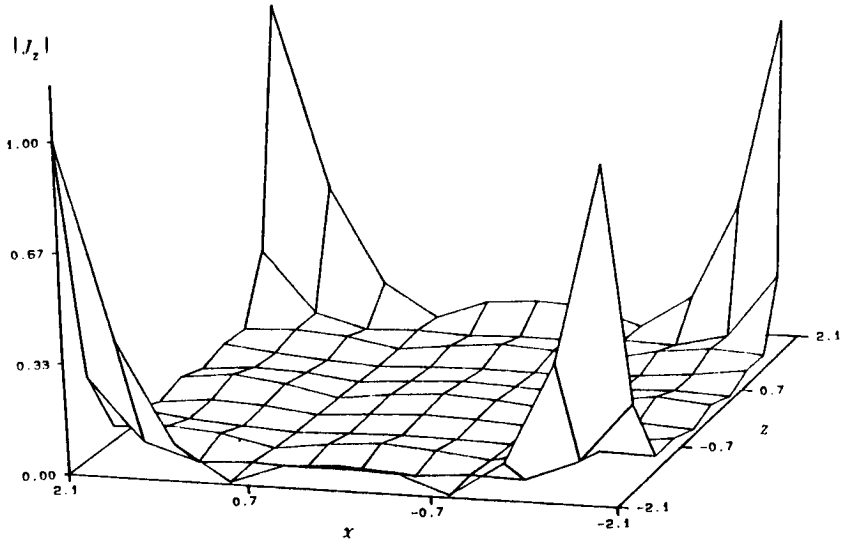

Figure 11.7 Equivalent current J_z for 2×2 dipoles on a $4\lambda \times 4\lambda$ surface using planar scaning.

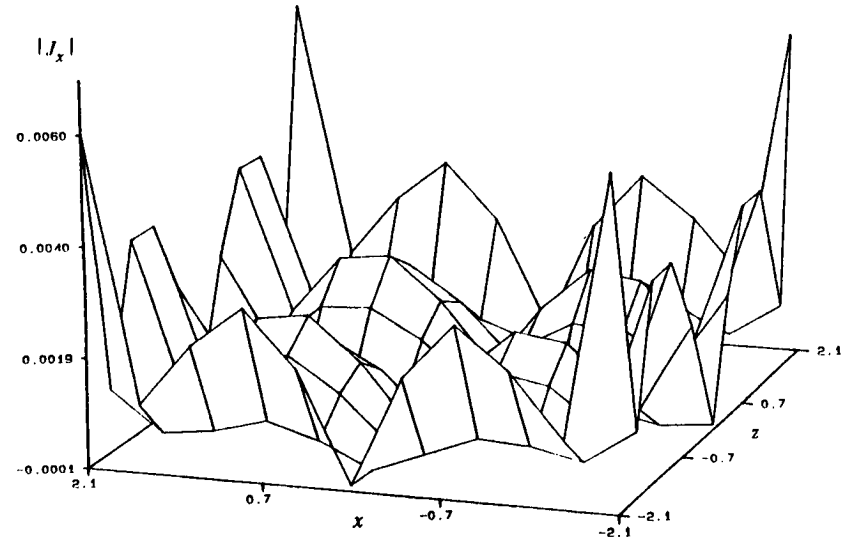

Figure 11.8 Equivalent current J_x for 2×2 dipoles on a $4\lambda \times 4\lambda$ surface using planar scaning.

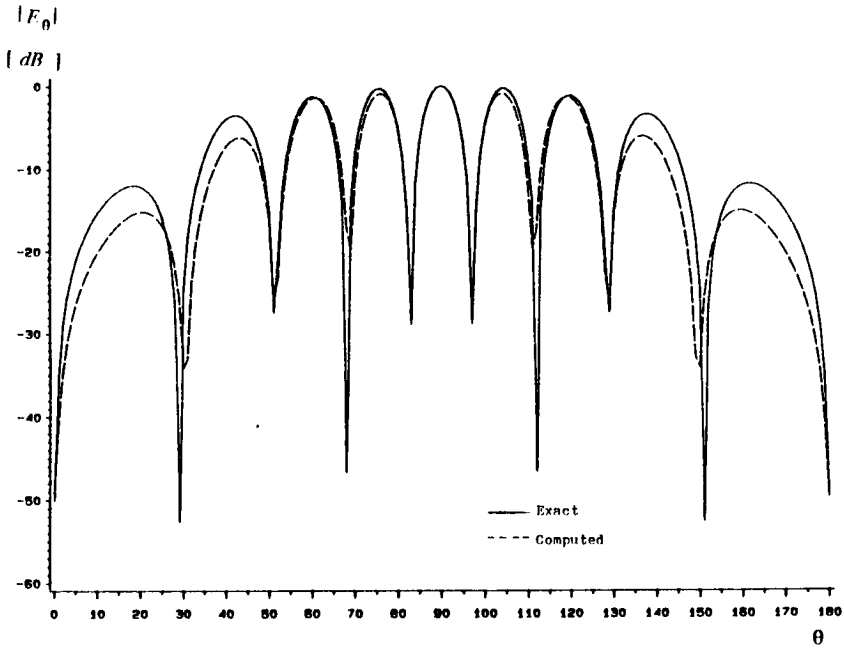

Figure 11.9 Comparison of exact and computed far-fields for $\phi = 90$ cut for 2×2 dipoles on a $4\lambda \times 4\lambda$ surface using parabolic scanning.

B. Sinusoidal Current Distribution

Consider a current distribution which is sinusoidal in the z-direction and constant in the x-direction, of the form

$$J_z(x,z) = \begin{cases} \sin(k(H-z)) & 0 \le z \le H, \quad \frac{-x_0}{2} \le x \le \frac{x_0}{2} \\ \sin(k(H+z)) & -H \le z \le 0, \quad \frac{-x_0}{2} \le x \le \frac{x_0}{2} \end{cases} \tag{59}$$

If H is an odd multiple of $\frac{\lambda}{4}$ then,

$$J_z(x,z) = \pm\cos(kz) \quad -H \le z \le H, \quad \frac{-x_0}{2} \le x \le \frac{x_0}{2} \tag{60}$$

To compute near-fields from this distribution, a closed form expression may be found for the z integration [17], and the x integration is performed using Gaussian quadrature [18]. For the distribution in (60) the far-field pattern is

$$F(\theta,\phi) = \frac{\cos[kH\cos\theta]}{\sin\theta} \; \frac{\sin\left[\frac{kx_0}{2}\sin\theta\cos\phi\right]}{\sin\theta\cos\phi} \tag{61}$$

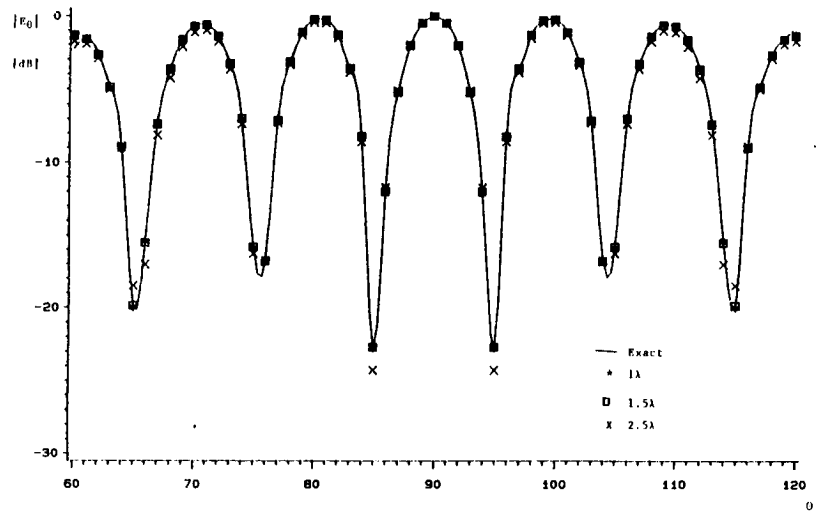

Figure 11.10 Comparison of exact and computed far-fields for $\phi = 90$ cut with varying discretizations for 2×2 dipoles on a $6\lambda \times 6\lambda$ surface using cylindrical scanning.

In the next few samples large antennas with a sinusoidal current distribution are studied.

Example 4

$$H = 2\frac{1}{4}\lambda, \quad x_0 = 0.5\lambda$$

Planar measurements:

$$XD_s = XD_f = \lambda, \quad ZD_s = ZD_f = 10\lambda$$
$$NXS = NXF = 21, \quad NZS = NZF = 189$$
$$d = 3\lambda$$

Figure 11.11 shows $|E_\theta|$ versus θ in dB for $\phi = 90°$. The results show excellent agreement between the computed and analytic results.

Example 5

$$H = 5\frac{1}{4}\lambda, \quad x_0 = 0.5\lambda$$

Planar measurements:

$$XD_s = XD_f = \lambda, \quad ZD_s = ZD_f = 20\lambda$$

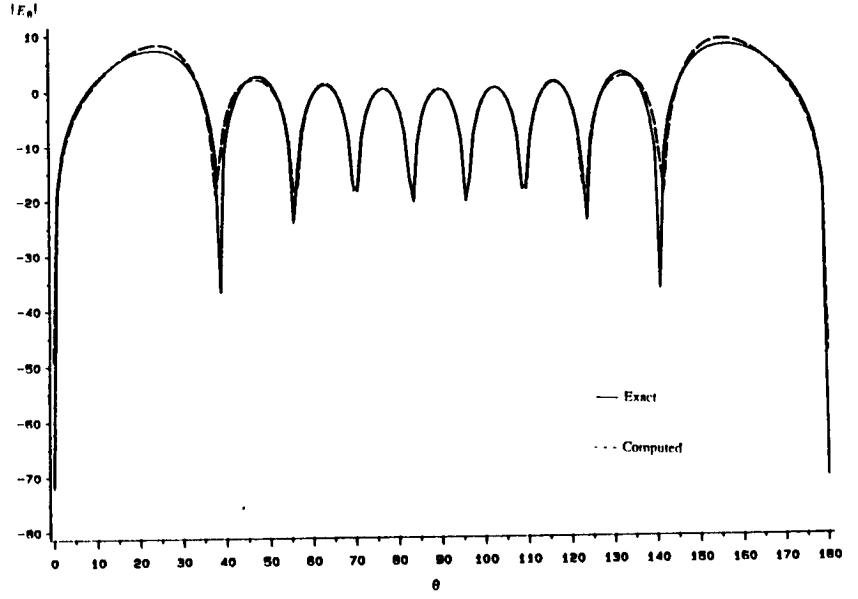

Figure 11.11 Comparison of exact and computed far-fields for $\phi = 90$ cut for $4.5\lambda \times \lambda/2$ surface with a sinusoidal current distribution.

$$NXS = NXF = 21, \quad NZS = NZF = 189$$
$$d = 3\lambda$$

Figure 11.12 shows $|E_\theta|$ versus θ in dB for $\phi = 90°$. The results show good agreement between the computed and analytic results, with slight discrepancies between 0 and 20° and 160° and 180°.

Example 6

$$H = 10\frac{1}{4}\lambda, \quad x_0 = 0.5\lambda$$

Planar measurements:

$$XD_s = XD_f = \lambda, \quad ZD_s = ZD_f = 40\lambda$$
$$NXS = NXF = 21, \quad NZS = NZF = 189$$
$$d = 3\lambda$$

Figure 11.13 shows $|E_\theta|$ versus θ in dB for $\phi = 90°$. The results show good agreement between the computed and analytic results, with discrepancies between 0 and 40° and 140° and 180°.

Example 7

$$H = 10\frac{1}{4}\lambda, \quad x_0 = 0.5\lambda$$

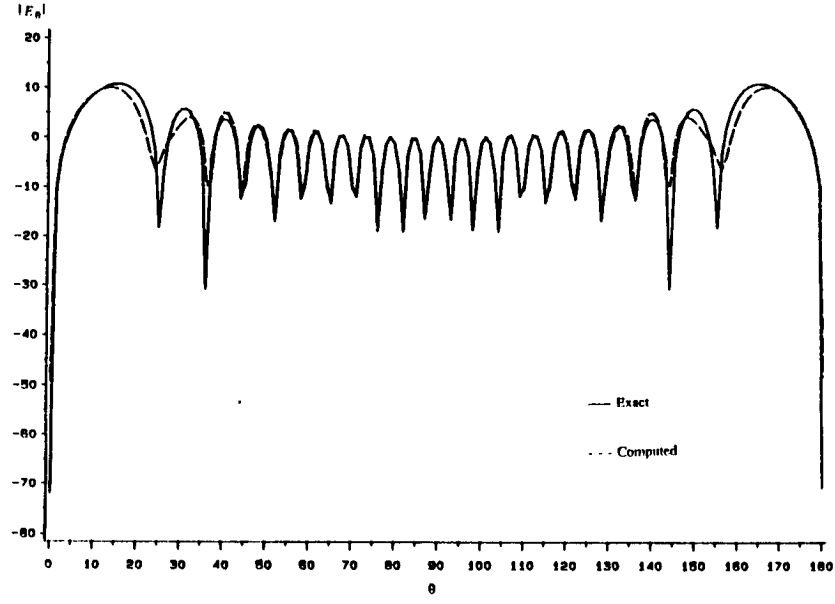

Figure 11.12 Comparison of exact and computed far-fields for $\phi = 90$ cut for $10.5\lambda \times \lambda/2$ surface with a sinusoidal current distribution.

Planar measurements:

$$XD_s = XD_f = \lambda, \quad ZD_s = ZD_f = 50\lambda$$
$$NXS = NXF = 21, \quad NZS = NZF = 1385$$
$$d = 3\lambda$$

In this example, the same antenna as in example 6 is used with more points sampled in the $z-$direction. Figure 11.14 shows $|E_\theta|$ versus θ in dB for $\phi = 90°$. The results show excellent agreement between the computed and exact far-fields.

C. Experimental Results

Consider a microstrip array consisting of 32 × 32 uniformly distributed patches on a 1.5 × 1.5 m surface. The near-fields are measured on a plane 3.24m × 3.24m at a distance of 35cm from the array. There

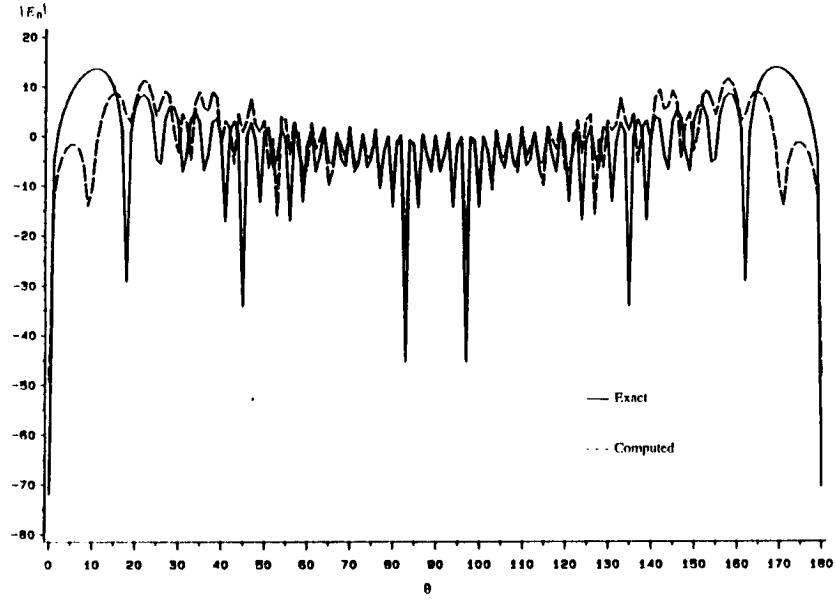

Figure 11.13 Comparison of exact and computed far-fields for $\phi = 90$ cut for $20.5\lambda \times \lambda/2$ surface with a sinusoidal current distribution.

are 81 × 81 points measures 4cm apart. The operating frequency is 3.3 GHz. The array is considered to be in the $x - y$ plane.

For the equivalent current approach, a 1.64m × 1.64m surface was used for both the source and field planes, with 41 × 41 current patches and field points. The probe is assumed to be an ideal Hertzian dipole.

For the planar modal expansion approach, 81 × 81 data points are zero-padded to produce 128 × 128 far-field points. Measurements are performed using a WR284 waveguide. For the spherical modal expansion approach, 360 theta and 90 phi points are measured with $\Delta\theta = 1°$ and $\Delta\phi = 2°$. The scan radius is 1.28m. There are 256 × 256 far-field points. Measurements are performed using an open ended cylindrical waveguide fed with the TE_{11} mode.

Figure 11.15 shows $|E_\theta|$ versus θ in dB for $\phi = 90°$ obtained using the current approach, along with results obtained using planar and spherical modal expansions. The two agree to within ±5dB for $-30° \leq$

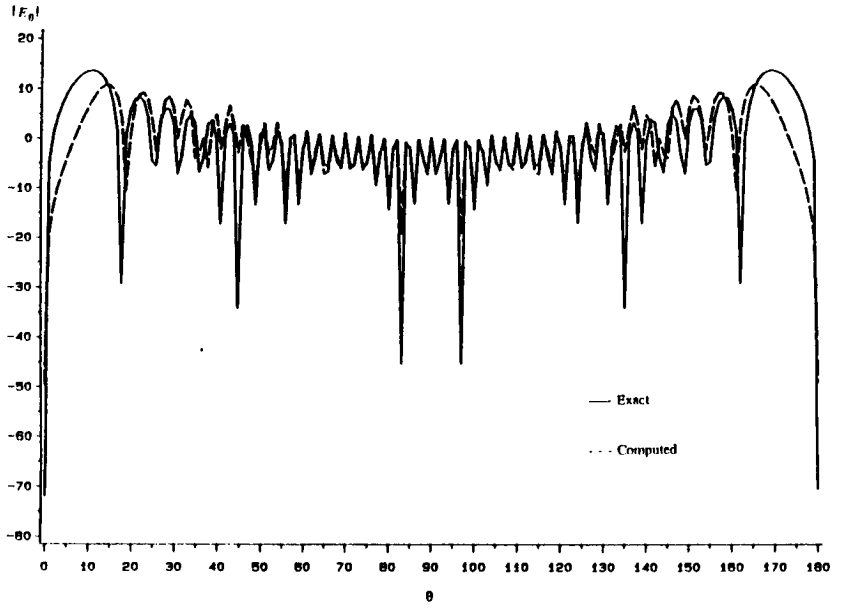

Figure 11.14 Comparison of exact and computed far-fields for $\phi = 90$ cut for $20.5\lambda \times \lambda/2$ surface with a sinusoidal current distribution.

$\theta \leq 30°$, however, beyond this the results deviate. It is clear from the plot that the results obtained with the planar modal expansion method diverge outside this region, since there should be nulls at $\pm 90°$. The nulls are apparent in the spherical modal expansion approach. The equivalent current approach gives deeper nulls and lower sidelobes than the spherical modal approach, however, the shape of the lobes is the same. A comparison with measured far-fields is required to conclusively determine which result is more accurate.

Probe compensation was implemented using (18) and (19). A pulse current was assumed to exist on the aperture of the waveguide, and the moment matrices Z_{aa}, Z_{ab} and Z_{bb} were computed. Figure 11.16 shows the principle cut with and without probe compensation. The results agree to within 3 dB. The similarity in results indicates that for this particular antenna, the induced currents are negligible.

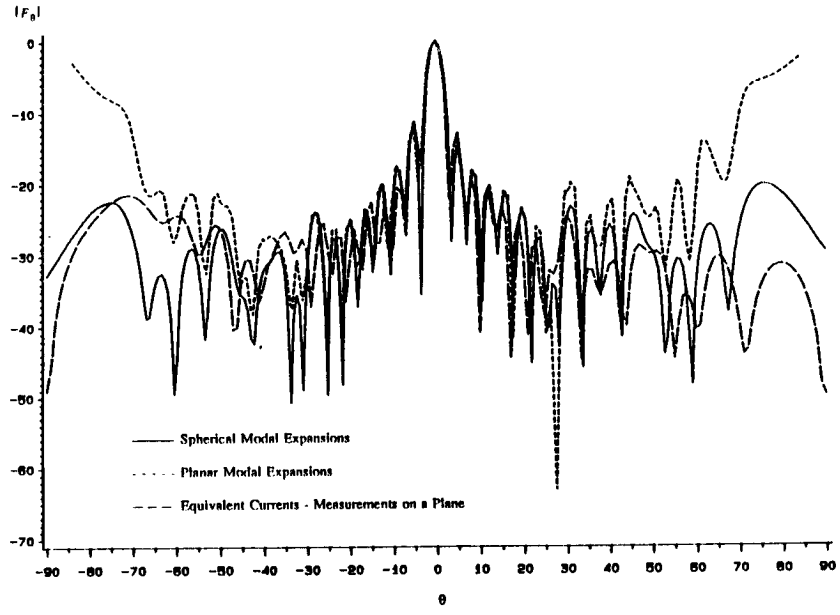

Figure 11.15 Comparison of far-fields obtained with planar and spherical modal expansions and using the equivalent current approach for $\phi = 90$ cut for a microstrip array.

11.6 Conclusion

A simple, accurate method is presented for computing far-fields from near-field data. The method can incorporate probe compensation which takes into account all induced currents and fields due to the presence of the probe. It is amenable to any measurement configuration, and the far-fields outside of the solid angle subtended by the measured region can be accurately approximated. Using this method it is possible to find the far-fields of antennas which are not highly directive over large elevation and azimuthal ranges without using spherical scanning. Furthermore, the far-field may be found with any desired resolution, and interpolation is not required. The maximum allowable sample spacing for some cases is shown to be greater than $\lambda/2$. For planar scanning using CGFFT, the equivalent current approach is com-

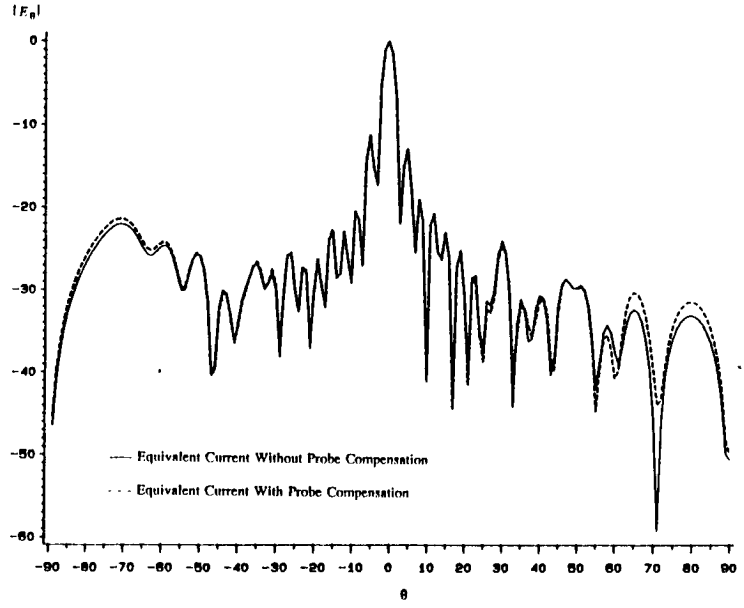

Figure 11.16 Comparison of far-fields obtained with probe compensation and without probe compensation for $\phi = 90$ cut for a microstrip array.

putationally efficient, and the order of computation is comparable to the planar and cylindrical modal expansion method.

Acknowledgment

The numerous expert technical suggestions of Dr. Tapan K. Sarkar are gratefully acknowledged. The author thanks Dr. Carl Stubenrauch for providing the experimental data, and the Cornell National Supercomputer Facility which was used to run some of the larger problems.

References

[1] Brown, J., and E. V. Jull, "The prediction of aerial radiation patterns from near-field measurements," *Proc. IEE,* **108B**, 635–644, 1961.

[2] Kerns, D. M., "Plane-wave scattering-matrix theory of antennas and antenna-antenna interactions," *NBS Monograph 162,* US Government Printing Office, 1981.

[3] Jensen, F., "Electromagnetic near-field far-field correlations," Ph.D. dissertation, Tech. Univ. Denmark, 1970.

[4] Wacker, P. F., "Near-field antenna measurements using a spherical scan: efficient data reduction with probe correction," *Inst. Elec. Eng. Conf. Publ. 113,* Conf. Precision Electromagn. Measurements, London, 286–288, July 1974.

[5] Wacker, P. F., "Non-planar field measurements: spherical scanning," *NBSIR 75-809,* June 1975.

[6] Leach, W. M., Jr., and D. T. Paris, "Probe-compensated near-field measurements on a cylinder," *IEEE Trans. Antennas Propagat.,* **AP-8021**, 435–445, July 1973.

[7] Yaghjian, A. D., "An overview of near-field antenna measurements," *IEEE Trans. Antennas Propagat.,* **AP-34**, 30–45, 1986.

[8] Appel-Hansen, J., "Antenna Measurements," *The Handbook of Antenna Design,* **1**, Perigrinus, London, 1982.

[9] Harrington, R. F., *Field Computation by Moment Methods,* Robert E. Kreiger Publishing, Malabar, 1968.

[10] Sarkar, T. K., E. Arvas, and S. M. Rao, "Application of FFT and conjugate gradient method for the solution of electromagnetic radiation from electrically large and small conducting bodies," *IEEE Trans. Antennas Propagat.,* **AP-34**, 635–640, 1986.

[11] Harrington, R. F., *Time Harmonic Electromagnetic Fields,* New York, McGraw-Hill, 1961.

[12] Paris, D. T., W. M. Leach and E. B. Joy, " Basic theory of probe-compensated near-field measurements," *IEEE Trans. Antennas Propagat.,* **AP-33**, 1058–1066, 1985.

[13] Collin, R. P., and F. J. Zucker, *Antenna Theory*, Part I, McGraw-Hill, New York, 1969.

[14] Sarkar, T. K., and E. Arvas, "On a class of finite step iterative methods (conjugate directions) for the solution of an operator equation arising in electromagnetics," *IEEE Trans. Antennas Propagation,* **AP-33,** 1058–1066, 1985.

[15] Oppenheim, A. V., and R. W. Shafer, *Digital Signal Processing*, Prentice-Hall, Englewood Cliffs, NJ, 1975.

[16] Newell, A. C., and M. L. Crawford, "Planar near-field measurements on high performance array antennas," *NBS Monograph 74-380*, U.S. Government Printing Office, Washington, DC, 1974.

[17] Jordan, E. C., and K. G. Balmain, *Electromagnetic Waves and Radiating Systems*, Prentice Hall, Englewood Cliffs, NJ, 1968.

[18] Abramowitz, M., and I. E. Stegun, *Handbook of Mathematical Functions*, National Bureau of Standards AMS 55, 1972.